

Elastic membranes of close-packed nanoparticle arrays

KLARA E. MUEGGENBURG¹, XIAO-MIN LIN², RODNEY H. GOLDSMITH¹ AND HEINRICH M. JAEGER^{1*}

¹James Franck Institute and Department of Physics, The University of Chicago, 929 E. 57th St., Chicago, Illinois 60637, USA

²Center for Nanoscale Materials, Argonne National Laboratory, 9700 South Cass Ave., Argonne, Illinois 60439, USA

*e-mail: h-jaeger@uchicago.edu

Published online: 22 July 2007; doi:10.1038/nmat1965

Nanoparticle superlattices are hybrid materials composed of close-packed inorganic particles separated by short organic spacers. Most work so far has concentrated on the unique electronic, optical and magnetic behaviour of these systems^{1–5}. Here, we demonstrate that they also possess remarkable mechanical properties. We focus on two-dimensional arrays of close-packed nanoparticles^{6,7} and show that they can be stretched across micrometre-size holes. The resulting free-standing monolayer membranes extend over hundreds of particle diameters without crosslinking of the ligands or further embedding in polymer. To characterize the membranes we measured elastic properties with force microscopy and determined the array structure using transmission electron microscopy. For dodecanethiol-ligated 6-nm-diameter gold nanocrystal monolayers, we find a Young's modulus of the order of several GPa. This remarkable strength is coupled with high flexibility, enabling the membranes to bend easily while draping over edges. The arrays remain intact and able to withstand tensile stresses up to temperatures around 370 K. The purely elastic response of these ultrathin membranes, coupled with exceptional robustness and resilience at high temperatures should make them excellent candidates for a wide range of sensor applications.

The combination of organic molecules and inorganic nanoparticles into hybrid materials offers a number of advantages for tailoring structural and functional properties by design^{5,8}. Incorporation of nanoparticles into polymeric thin films can significantly improve their thermomechanical properties⁹. Thin-film membranes, with nanoparticles sandwiched into the centre of polymer multilayers^{10,11} or comprising interpenetrating organic/inorganic networks¹², show enhanced strength and robustness that allow for applications ranging from separation membranes to high-resolution pressure sensors. In such nanocomposites, the volume fraction of embedded nanoparticles typically is small, their arrangement is random, and the polymer chains comprising the matrix are long enough to entangle. Here, we investigate the elastic properties for the opposite limit, where the nanoparticles are in compact, close-packed arrangements and are separated by short spacer molecules.

Lin *et al.* showed that crosslinked ultrathin nanoparticle sheets of this type crumple like thin sheets of paper⁶, whereas Lee *et al.* recently reported viscoplastic behaviour in CdSe nanoparticle films hundreds of particles thick¹³ and Klajn *et al.* found plastic behaviour in three-dimensional (3D) superstructures built out of metal nanoparticles¹⁴. In these experiments, however, the local particle packing configurations were not known or hard to control, and thicker films exhibited inhomogeneities and cracks. The

approach described here circumvents these difficulties by self-assembling the nanoparticle monolayer at a liquid–air interface and draping it over a solid substrate with prefabricated holes. Once dried onto the substrate, the array portion stretched across the holes forms free-standing membranes. The self-assembly provides for well-ordered close-packed particle arrangements, whereas the circular edge of the holes establishes well-defined boundary conditions for testing the membrane's elastic properties by indenting it at the centre. This makes such monolayers a model system to investigate the ultrathin limit of nanoparticle-based membranes.

In our experiments, 2D arrays are formed by letting dodecanethiol-ligated gold nanocrystals suspended in toluene spread across the top of a water droplet resting on a silicon nitride substrate (see the Methods section). As the water evaporates, the monolayer drapes itself over the substrate with the holes (Fig. 1). Within our experimental resolution, the average interparticle spacing, ~ 1.4 nm, and the degree of local ordering inside the hole are indistinguishable from what we observe on the surrounding substrate (Fig. 1b). The latter point is demonstrated nicely by tilting the plan-view image and tracing the particle lattice into the hole region (Fig. 1c). Atomic force microscopy (AFM) shows that the monolayer inside the hole is flat and smooth, but recessed below the silicon nitride surface (Fig. 1d–f) to a depth of 35–100 nm or roughly 4–12 particles. We note that these membranes self-assemble in a single processing step and do not require crosslinking or further chemical treatment to be stable. The results discussed below are based on measurements on 33 different monolayer membranes, each estimated to be ~ 9.4 nm thick (the diameter of a single nanoparticle, 6 nm, plus twice the length of the ligand¹⁵, 1.7 nm) and with diameters ranging from 500 to 2,200 nm.

To study their elastic properties, we indented the monolayer membranes at their centre with an AFM tip (Fig. 2a). Figure 2b shows a typical trace of the resulting force–displacement curve. All curves are linear in force, F , for small indentations, δ , but turn nonlinear as δ significantly exceeds the membrane thickness, h . The indenting and retracting curves overlap in the downward-displacement ($\delta > 0$) regime, indicating that the membrane responds elastically. The hysteresis in the upward-displacement ($\delta < 0$) region is due to adhesion between the tip and the membrane probably dominated by water-meniscus effects. In contrast to results for thicker films¹³ and membranes¹¹, $F(\delta)$ in our arrays does not depend on tip speed and we find no evidence for viscoplastic effects (see Supplementary Information, Fig. S2). Although each indent/retract cycle reaches displacements $\delta \gg h$ and induces strains up to 1.5%, as estimated from a conical stretching geometry,

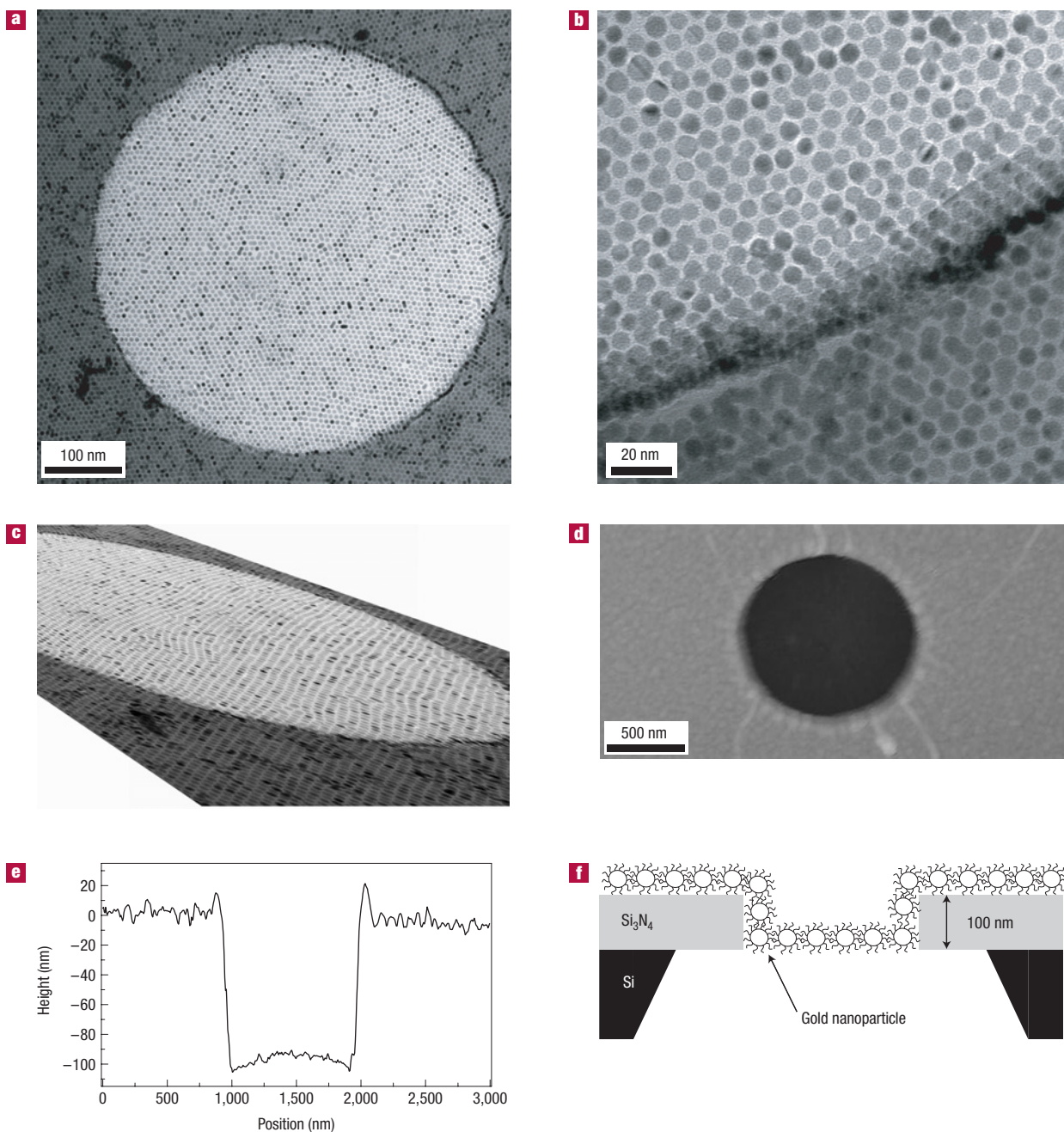


Figure 1 Self-assembled ultrathin nanoparticle membranes. Two free-standing arrays are shown: a smaller one with a radius of 250 nm (**a,c**) and a larger one with a radius of 550 nm (**b,d,e**). **a**, TEM image of a gold nanoparticle monolayer freely suspended over a hole with a 250 nm radius in the silicon nitride substrate. An optical micrograph of the arrangement of all holes in a given substrate is shown in Supplementary Information, Fig. S1. **b**, Higher magnification TEM of a membrane with a radius of 550 nm. **c**, Image in **a** tilted to show the close-packed order of the nanoparticles inside and outside the hole. **d**, AFM height image of the same array as in **b**. The darker colour inside the hole indicates that the membrane is recessed. **e**, Cross-section of the height image in **c**. **f**, Schematic diagram of the array configuration inside a single hole. The array recedes into the hole almost the same distance as the thickness of the silicon nitride. The projection of nanoparticles on the vertical wall of the hole shows up as a dark band at the edge in **a** and **b**.

we observe no permanent damage even after repeated indentations (Figs 1d and 3a).

We find that the overall stiffness of the membranes decreases monotonically with increasing hole radius, R (Fig. 2c). We quantify this by plotting the equivalent spring constant in the linear regime, $k = dF/d\delta$, as a function of the membrane radius, R , for three separate sets of experiments, each using a different batch

of nanoparticles (Fig. 2d). Point-force elastic theory predicts^{16,17} $k \sim 1/R^2$, as shown by the solid line in Fig. 2d. Theories that include the effects of a finite indenter radius predict¹⁸ $k \sim 1/R^{3/4}$ (dashed line). Within experimental uncertainty, our data are compatible with both. We believe that the variations between data sets seen in Fig. 2d are due to different degrees of pre-stretch induced in the final drying stage of the membranes

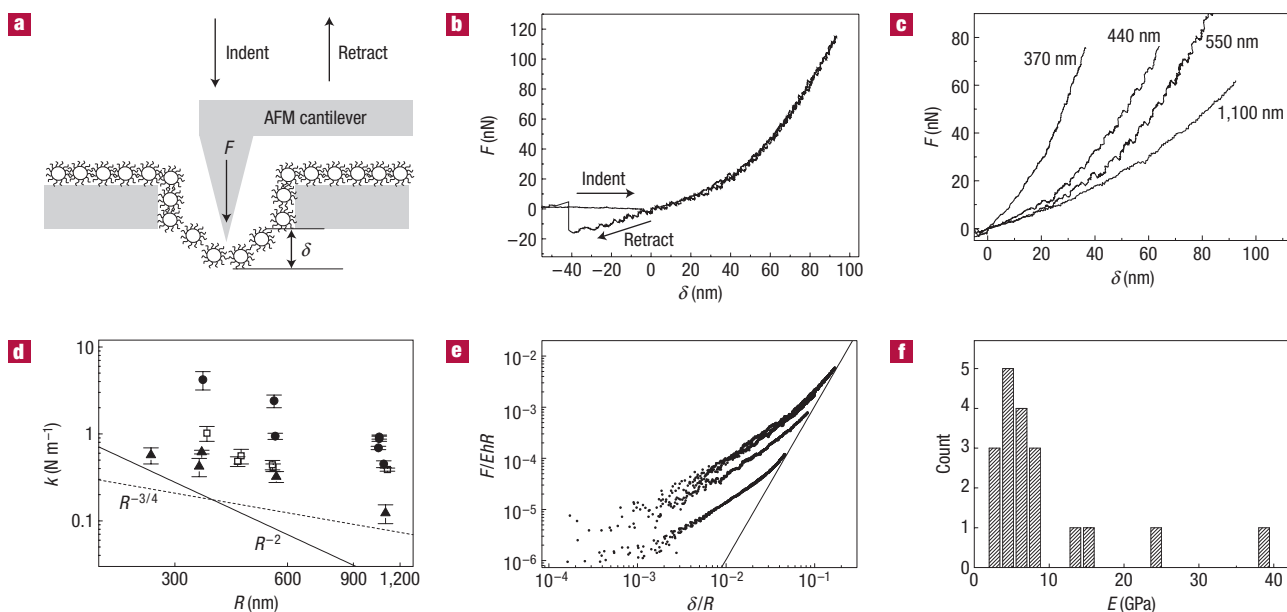


Figure 2 Indentation response. **a**, Schematic diagram: as an AFM tip exerts a force on the membrane the vertical displacement is measured. **b**, Force, F , as a function of displacement, δ , for the array in Fig. 1b. No hysteresis and thus no plastic deformation is observed for positive, downward displacement. **c**, Force curves for membranes with different radii, R , as indicated. **d**, Spring constant, $k = dF/d\delta$ of membranes in the small-displacement regime. Different symbols represent samples from different nanoparticle batches. Statistical error bars from 5–15 force curves for each point are shown. For comparison, the lines show the power-law dependence of k on R on the basis of the elastic theory of point-force indentation^{16,17} (solid line) and of a spherical indenter¹⁸ (dashed line). **e**, Rescaled log–log plot of force curves for five different membranes (including the four shown in **c**). The parameter values are radius $R = 440, 550, 370, 1,110, 1,100$ nm and Young's modulus $E = 4.3, 3.8, 13, 7.6, 39$ GPa (top to bottom); the thickness $h = 9.4$ nm for all membranes. In this type of plot, elastic theory predicts force curves to cross over from a linear regime, where k depends on both pre-stretch and Young's modulus, to a cubic regime with a large-displacement asymptote (solid line) that is independent of pre-stretch¹⁷. **f**, Histogram of Young's moduli derived from large-displacement asymptotes, as in **e**. In all panels, the data shown are not averaged. Data in **c–e** are the indent branch only.

or small differences in the ligand concentration from batch to batch.

Analysing the force curves within the framework of elasticity theory^{16,17} for homogeneous membranes, we can extract an effective Young's modulus, E . As k depends sensitively on pre-stretch, which *a priori* is unknown, k cannot be used to determine E . However, for larger displacements, where the stretching energy dominates, all force curves are predicted to converge onto the same asymptotic behaviour, regardless of pre-stretching^{16,17}. Assuming a Poisson ratio of 1/3 and the application of a point force, this asymptote has the form

$$F = \frac{\pi E h}{3R^2} \delta^3. \quad (1)$$

In line with numerical predictions¹⁷, the crossover from linear to cubic $F \sim \delta^3$ dependence is found in our experiments when δ becomes a sizeable fraction of the membrane radius (Fig. 2e). We note that in most other experiments^{10,11} it has been difficult to capture this crossover, and one has to rely on data obtained with different techniques, such as bulge tests for large deflections.

Equation (1) predicts that plots of force, scaled as F/EhR , versus normalized displacement, δ/R , should approach a single universal asymptote. From such plots, E can be determined by adjusting the scaling such that the experimental curve asymptotes to the theoretical line (Fig. 2e). Results from 19 membranes in which δ was large enough to approach the asymptotic regime give an E value in the range of 3–39 GPa with a median of 6 GPa (Fig. 2f). The scatter around this median is due to both uncertainties in finding the asymptote and compositional differences in membranes made from different nanoparticle

batches. Relaxing the point-force assumption and taking the indenter radius of curvature, r , into account¹⁸ modifies the right-hand side of equation (1) by a factor $(r/R)^{1/4}$. Using the radii of our AFM tips as measured by scanning electron microscopy, we find that this changes the results for E by less than 40%, which is well within the statistical spread.

From the values for E together with the results for k , we can determine *a posteriori* the level of pre-stretch in the membranes, using the analysis developed in ref. 16. Our data indicate pre-strain levels between 0.02% and 0.6% (see Supplementary Information, Fig. S3). Calculations on the basis of ref. 18 yield similar results. These values are smaller than those observed in 3D films¹⁹, but the origin of the pre-strain is probably the drying process just as in the thick films.

The large effective Young's modulus, similar to that of glassy polymers, is remarkable for a single sheet of nanoparticles embedded in short-chain molecules. With equilibrium chain lengths¹⁵ of ~ 1.7 nm and interparticle spacing of ~ 1.4 nm, dodecanethiol ligands from neighbouring particles overlap, and possibly interdigitate²⁰. Considering only the attractive London–van der Waals interactions between the metal spheres, as derived by Hamaker²¹, gives k values of less than 10% of what we observe. This means that the ligands function not merely as mechanical spacers counteracting the core-to-core attraction but also provide the tensile strength of the array through ligand–ligand interactions. We can estimate the effective modulus of the ligand portion, E_{thiol} , of the composite by using theories of elastic properties of composite media with random filler distributions²² and the known bulk and shear moduli for crystalline gold²³. This gives $E_{\text{thiol}} \sim 4$ GPa, which is larger than E of most polymers²⁴, including polyethylene and

poly(methyl methacrylate). In polymers the Young's modulus is a direct result of the entanglement of long-chain molecules. The dodecanethiol ligands on the nanoparticle surfaces are too short to entangle and the large Young's modulus is a consequence of the confinement of the ligand to the nanoparticle surfaces and to the spaces between the particles.

A large overall Young's modulus due to ligand confinement and concomitant interactions is consistent with the work of Landman and Luedtke who found $E \sim 1$ GPa in molecular dynamics simulations of 3D superlattices of dodecanethiol-ligated gold particles²⁰. These simulations also find that almost all of the attractive potential in the superlattices comes from van der Waals interactions between ligands that are confined to the interstices between neighbouring nanoparticles. Our results are also comparable to the moduli of around 8–12 GPa reported for thick, essentially 3D, trioctylphosphine-oxide-coated CdSe nanoparticle films¹³ and to $E \sim 3$ GPa for the 3D metal nanoparticle aggregates¹⁴.

Ultrathin membranes possess several properties that reflect their unique, effectively 2D nature. One is increased bending flexibility. As seen in Fig. 1, the monolayer easily accomplishes two sharp bends as it drapes itself over the edge of the hole and then again before it stretches across. Whereas the AFM trace (Fig. 1e) does not provide sufficient resolution as it convolutes the topology with tip shape, the transmission electron microscope (TEM) image (Fig. 1b) shows that these two right-angle bends occur over just a few particle diameters. Such combination of extreme flexibility with high tensile strength is reminiscent of articulated 2D structures such as nets or chain mail.

Another remarkable feature is the resilience at elevated temperatures. Testing eight of our membranes on a high-temperature AFM stage, we find that they withstand repeated indentation up to at least 330 K in air and typically show significant damage only above 370 K (Fig. 3), the temperature where gold particles start to sinter. Interestingly, up to about 370 K initial damage of the membrane shows up as local rips or tears at pre-existing weak spots, rather than as uniform weakening or melting.

Furthermore, as long as the membrane stays intact sufficiently to carry out AFM measurements, within the experimental uncertainties, increasing temperature does not reduce the low-force stiffness k significantly (see Supplementary Information, Fig. S4). These results at first glance seem at variance with simulations in ref. 20 that predict surface ligand melting around 312 K and a vanishing Young's modulus around 350 K for 3D dodecanethiol-ligated gold superlattices. However, the membrane stiffness depends on pre-stretch as well as on E . As our free-standing membranes have a pinned edge, the interparticle spacing is not allowed to decrease even though ligands contract with increasing temperature^{20,25}. The resulting increase in pre-stretch can then compensate for the temperature-induced reduction in Young's modulus to result in an approximately constant k . In addition, the tendency to rip and the absence of significant softening suggests that the melting temperature might be shifted upwards in ultrathin membranes. We speculate that this could be due to enhanced ligand confinement into the plane of the particles.

In summary, we have demonstrated that free-standing, ultrathin arrays of close-packed nanoparticle monolayers can be self-assembled on silicon wafers in a single processing step. Consisting of a single layer of the fundamental building blocks of the material, the passivated nanoparticles, these membranes reach the ultimate thickness limit of an artificial solid. The arrays combine extreme bending flexibility with high tensile strength. Their effective Young's moduli rival those of 3D nanoparticle films and of much thicker particle-embedded polymer multilayers. This surprisingly large E appears to be due to the ligand molecules that are too short to entangle like polymers but interact strongly

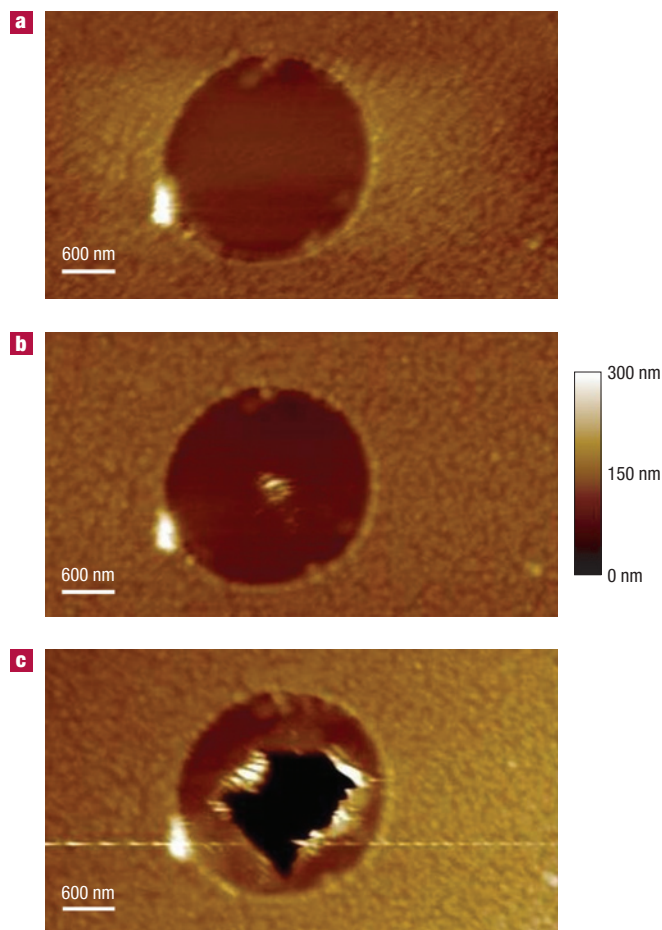


Figure 3 Membrane resilience at elevated temperatures. AFM tapping mode images of a 2- μm -diameter membrane at different temperatures. **a**, At 298 K; after force–displacement measurements were taken. **b**, At 373 K; the array did not melt nor tear even though a weak spot, and possibly a small hole, appeared where the force measurements stressed the array. **c**, At 413 K; the array has failed by ripping. Nevertheless, large portions of it still appear intact and stretched flat across the hole.

when confined to the interstices between nanoparticles. Their robustness should make these arrays well suited for a wide range of applications that depend on ultrathin free-standing membranes. It should also allow for studies of substrate-free optical and electronic properties of nanoparticle superlattices. Unlike most polymers, close-packed nanoparticle arrays conduct electricity by electron tunnelling²⁶. As the tunnel resistance is exponentially dependent on changes in the interparticle spacing, this makes these structures candidates for high-sensitivity electronic pressure sensors.

METHODS

FABRICATION

3 mm \times 4 mm silicon wafer chips coated with 100 nm silicon nitride were used as substrates. At two spots near the centre of each chip, the silicon was etched away from the back to create 100-nm-thick TEM-transparent silicon nitride ‘window’ areas, 70 μm \times 70 μm (ref. 27). Circular holes with diameters ranging from 400 nm to 2 μm were cut into each silicon nitride window using electron-beam lithography and reactive ion etching (see Supplementary Information, Fig. S1). Dodecanethiol-ligated gold nanoparticles with an average diameter of 6 nm were synthesized using the digestive ripening protocol²⁸ and suspended in toluene. Five different synthesis batches were used

in the experiments. The size dispersion of the particles was <8% within each batch and <20% from batch to batch.

Compact well-ordered nanoparticle monolayers formed at the water–air interface when the nanoparticle suspension was deposited onto a drop of water resting on the substrate²⁹. In our experiments, 20 μl of suspension (concentration $\sim 10^{13}$ particles ml^{-1}) was deposited on top of 8 μl of water, and monolayers formed readily within minutes. After the toluene evaporated, the substrate with the water drop was lifted onto a mesh to dry. The resulting dry free-standing arrays were stable in air over days. A total of 33 intact membranes were investigated with diameters in the range of 500–2,200 nm. As the diameter increased, the fraction of arrays that tore during the fabrication increased. Because of the decreased yield, we did not try to suspend arrays over holes bigger than 2.2 μm . Dodecanethiol, which in bulk is a liquid at room temperature, does not suspend over the holes by itself; ligand confinement to the nanoparticle surfaces is necessary for the mechanical stability of free-standing arrays. AFM height measurements of monolayers on a solid surface gave a thickness of ~ 7 –8 nm, which is an underestimate of the free-standing membrane thickness because of attractive interactions between the array and the solid surface.

CHARACTERIZATION AND MEASUREMENTS

High-resolution structural characterization was carried out using a Tecnai F30 TEM. To limit potential effects from electron irradiation, TEM imaging was done after AFM force measurements. Veeco Nanoscope III and Nanoscope IV AFMs were used for extracting force–displacement curves and, in tapping mode, for imaging. We used force modulation silicon cantilevers with spring constants ranging from 0.5 to 3 N m^{-1} . The spring constant for each tip was calculated using a rectangular beam model after measuring the cantilever dimensions with an optical microscope and a scanning electron microscope. The cantilever tips were imaged by scanning electron microscopy to estimate the radii of curvature, which ranged from 50 to 240 nm in the region that is likely to be in contact with the membrane. Typical maximum applied forces were ~ 100 nN at maximum indentations of ~ 80 nm. The indentation speed was varied from 30 to 3,500 nm s^{-1} without observing significant differences in the response (see Supplementary Information, Fig. S2). The typical tip speed for the data shown in Fig. 2 was 500 nm s^{-1} . Each membrane was first imaged by AFM, then indented about a hundred times while 5–15 force curves were recorded, and finally was imaged again to check for damage. When measurements were repeated 18 h later, we found no detectable difference.

To study the temperature dependence, we used a Veeco Nanoscope III AFM with a high-temperature stage, water-cooled scanner and silicon cantilevers with spring constants of 0.5–0.8 N m^{-1} . The temperature was increased in increments of 20 $^{\circ}\text{C}$ at rates of 20 $^{\circ}\text{C min}^{-1}$ and the samples were allowed to equilibrate for at least 10 min before data taking (longer waiting times, up to 1 h, yielded the same results). The highest temperatures applied were typically limited to around 140 $^{\circ}\text{C}$ but in some instances were extended to 180 $^{\circ}\text{C}$, depending on when a membrane failed. After AFM measurements, the membranes were examined by TEM.

Received 26 March 2007; accepted 12 June 2007; published 22 July 2007.

References

- Murray, C. B., Kagan, C. R. & Bawendi, M. G. Self-organization of CdSe nanocrystallites into three-dimensional quantum-dot superlattices. *Science* **270**, 1335–1338 (1995).
- Pileni, M. P. Nanosized particles made in colloidal assemblies. *Langmuir* **13**, 3266–3276 (1997).

- Puntes, V. F., Krishnan, K. M. & Alivisatos, A. P. Colloidal nanocrystal shape and size control: The case of cobalt. *Science* **291**, 2115–2117 (2001).
- Shevchenko, E. V., Talapin, D. V., Kotov, N. A., O'Brien, S. & Murray, C. B. Structural diversity in binary nanoparticle superlattices. *Nature* **439**, 55–59 (2006).
- Lopes, W. A. & Jaeger, H. M. Hierarchical self-assembly of metal nanostructures of diblock copolymer scaffolds. *Nature* **414**, 735–738 (2001).
- Lin, Y. *et al.* Ultrathin cross-linked nanoparticle membranes. *J. Am. Chem. Soc.* **125**, 12690–12691 (2003).
- Bigioni, T. P. *et al.* Kinetically driven self assembly of highly ordered nanoparticle monolayers. *Nature Mater.* **5**, 265–270 (2006).
- Balazs, A. C., Emrick, T. & Russell, T. P. Nanoparticle polymer composites: Where two small worlds meet. *Science* **314**, 1107–1110 (2006).
- Liff, S. M., Kumar, N. & McKinley, G. H. High-performance elastomeric nanocomposites via solvent-exchange processing. *Nature Mater.* **6**, 76–83 (2007).
- Jiang, C., Markutsya, S., Pikus, Y. & Tsukruk, V. Freely suspended nanocomposite membranes as highly sensitive sensors. *Nature Mater.* **3**, 721–728 (2004).
- Markutsya, S., Jiang, C., Pikus, Y. & Tsukruk, V. V. Freely suspended layer-by-layer nanomembranes: Testing micromechanical properties. *Adv. Funct. Mater.* **15**, 771–780 (2005).
- Vendamme, R., Onoue, S.-Y., Nakao, A. & Kunitake, T. Robust free-standing nanomembranes of organic/inorganic interpenetrating networks. *Nature Mater.* **5**, 494–501 (2006).
- Lee, D. *et al.* Viscoplastic and granular behavior in films of colloidal nanocrystals. *Phys. Rev. Lett.* **98**, 026103 (2007).
- Klajn, R. *et al.* Plastic and moldable metals by self-assembly of sticky nanoparticle aggregates. *Science* **316**, 261–264 (2007).
- Bain, C. D. *et al.* Formation of monolayer films by the spontaneous assembly of organic thiols from solution onto gold. *J. Am. Chem. Soc.* **111**, 321–335 (1989).
- Wan, K.-T., Guo, S. & Dillard, D. A. A theoretical and numerical study of a thin clamped circular film under an external load in the presence of a tensile residual stress. *Thin Solid Films* **425**, 150–162 (2003).
- Komaragiri, U., Begley, M. R. & Simmonds, J. G. The mechanical response of freestanding circular elastic films under point and pressure loads. *J. Appl. Mech.* **72**, 203–212 (2005).
- Begley, M. R. & Mackin, T. J. Spherical indentation of freestanding circular thin films in the membrane regime. *J. Mech. Phys. Solids* **52**, 2005–2023 (2004).
- Banerjee, S. *et al.* Raman microprobe analysis of elastic strain and fracture in electrochemically deposited CdSe nanocrystal films. *Nano Lett.* **6**, 175–180 (2006).
- Landman, U. & Luedtke, W. D. Small is different: Energetic, structural, thermal and mechanical properties of passivated nanocluster assemblies. *Faraday Discuss.* **125**, 1–22 (2004).
- Hamaker, H. C. The London–van der Waals attraction between spherical particles. *Physica* **4**, 1058–1072 (1937).
- Kerner, E. H. The elastic and thermo-elastic properties of composite media. *Proc. Phys. Soc. London B* **69**, 808–813 (1956).
- Collard, S. M. & McLellan, R. B. High-temperature elastic constants of gold single-crystals. *Acta Metall. Mater.* **39**, 3143–3151 (1991).
- Mark, J. E. *Polymer Data Handbook* (Oxford Univ. Press, New York, 1999).
- Luedtke, W. D. & Landman, U. Structure, dynamics, and thermodynamics of passivated gold nanocrystallites and their assemblies. *J. Phys. Chem.* **100**, 13323–13329 (1996).
- Parthasarathy, R., Lin, X.-M. & Jaeger, H. M. Electronic transport in metal nanocrystal arrays: The effect of structural disorder on scaling behavior. *Phys. Rev. Lett.* **87**, 186807 (2001).
- Morkved, T. L., Lopes, W. A., Hamm, J., Sibener, S. J. & Jaeger, H. M. Silicon nitride membrane substrates for the investigation of local structure in polymer thin films. *Polymer* **39**, 3871–3875 (1998).
- Lin, X.-M., Sorensen, C. M. & Klabunde, K. J. Digestive ripening, nanophase segregation and superlattice formation in gold nanocrystal colloids. *J. Nanopart. Res.* **2**, 157–164 (2000).
- Eah, S.-K. 2006 *Materials Research Society Fall Meeting Abstracts* 401 (Materials Research Society, Warrendale, 2006).

Acknowledgements

We thank W. D. Luedtke, S. Nagel, T. Witten, W. Lopes, T. Tran and L. Adams for helpful discussions, Q. Guo and X. Liao for technical assistance and S.-K. Eah for sharing the water-depositing technique. This work was supported by the UC-ANL Consortium for Nanoscience Research and by the NSF MRSEC program under DMR 0213745. R.H.G. was supported by the MRSEC REU program during his stay at the University of Chicago. X.-M.L. acknowledges support from the US DOE, BES-Materials Sciences, under Contract DE-AC02-06CH11357. Correspondence and requests for materials should be addressed to H.M.J. Supplementary Information accompanies this paper on www.nature.com/naturematerials.

Competing financial interests

The authors declare no competing financial interests.

Reprints and permission information is available online at <http://npg.nature.com/reprintsandpermissions/>